Deep Regression for Imaging Solar Magnetograms using Pyramid Generative Adversarial Networks

Rasha Alshehhi
New York University, Abu Dhabi
Abu Dhabi, United Arab Emirates
ra130@nyu.edu

Abstract

Monitoring a large active region in the farside of the Sun is important for space weather forecasting. However, direct imaging of the farside is currently not available and usually physicists rely on seismic holography to infer farside magnetograms. On other hand, mapping between holography and magnetic images is non-trivial. In this work, Generative Adversarial Network (GAN) is used; which consists of a pyramid of modified pixel2pixel architectures to capture internal distributions at different scales with higher quality. Generative model is trained and evaluated using frontside of Solar Dynamic Observatory (SDO): Atmospheric Imaging Assembly (AIA) and Helioseismic and Magnetic Imager (HMI) magnetograms. Farside solar magnetograms from Extreme UltraViolet Imager (EUVI) farside data is also generated. The generative model successfully generates frontside solar magnetograms and outperforms state-of-the art method. It also help to monitor the magnetic changes from farside to frontside using generated solar magnetograms.

1. Introduction

Active regions in the Sun are areas with strong magnetic field. They are centers of energetic phenomena (e.g., solar flares and coronal mass ejections); which result electromagnetic and particle radiation interfere with telecommunications and power transmission on the Earth and can cause significant hazards to astronauts and spacecrafts. This impact on the Earth is predominately due to active regions in the Sun near hemisphere. However, the Sun rotates and active regions in the far hemisphere cross into near hemisphere. Therefore, NASA's twin Solar TErrestrial RElationship Observatory (STEREO) [9] spacecraft had been used to monitor the entirely of far hemisphere from the farside of Earth's orbit. This spacecraft was gradually drifting back to Earth's side of its orbit losing its coverage. As a result,

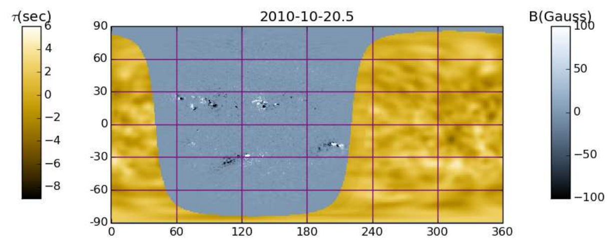

Figure 1. Composite maps of the Sun's far hemisphere holography map (yellow) and near hemisphere (blue gray) show a certain active region, from `http://jsoc.stanford.edu/data/farside/Phase_Maps/`

electromagnetic coverage of the Sun's far hemisphere is unavailable or incomplete. Therefore, astrophysicists develop algorithms based on seismic holography to continued monitor the sun far hemisphere. The holography imaging of nonvisible side of the Sun will allow anticipation of the appearance of large active regions more than a week ages ahead before they rotate to face the Earth [13, 14]. Consequently, monitoring active regions on the farside of the Sun would greatly improve long-time forecasting of space weather on the Earth. However, the quality of both STEREO and holography images are lower that typical frontside images. Figure 1 shows farside seismic maps (yellow); which has lower quality compared to frontside map (blue gray). In this work, Generative Adversarial Networks (GAN) [5] is used to predict frontside (blue gray) and then farside solar image (yellow) with higher quality.

Generative Adversarial Networks (GAN) [5] show remarkable success in modeling high dimensional distribution, capturing internal distribution of data with higher quality. They are used in different tasks such as image-to-image translation [8, 20], super-resolution [11, 19]. However, capturing distribution of highly diverse data with wide range in each data sample is still a major challenge and may need preprocssing/post-processing steps.

In this work, multi-layer conditional generative model is used to predict the true distribution of solar image of frontside and then for farside using PatchGAN [8]. Solar Dynamic Observatory (SDO) [16] data is used; which consists of a pair of Atmospheric Imaging Assembly (AIA) [12] and Helioseismic and Magnetic Imager (HMI) [1, 18], to train generative networks. AIA provides high-resolution full-disk images of the corona and transition region (chromoshpere) of Sun to study the characteristics of the Sun's dynamic magnetic field and how the corona respond to it. HMI provides high-resolution full-disk images of solar photosphere to study solar oscillations and understand the interior structure of Sun (HMI magnetogram called line-of-sight magnetic field image); see Section 4.1 for data description. The network is evaluated using SDO/AIA and SDO/HMI. The model is utilized to predict HMI magnetic field image of Extreme UltraViolet Imager (EUVI) [7] data of Solar TErrestrial RElationship Observatory (STEREO) [9]. STEREO/EUVI image is similar to SDO/AIA image, but with lower quality. The generator network is a series of generators, which are used to generate solar magnetogram (line-of-sight magnetic field image) from AIA and then from EUVI data of multi-resolutions. The discriminator network is also a multi-layer discriminator, used to distinguish between real pair (e.g, AIA and HMI magnetogram) and generated pair (AIA and generated HMI magnetogram).

This work is organized as follow. The related work will be described in Section 2 and the method in Section 3. Experimental analysis and results are presented in Section 4. Summary and future works are highlighted in Section 5.

2. Related Work

Many recent works use multi-scale generative architectures. T. Shaham *et. al* introduced SinGAN [19]. It is an unconditional generative network that can learn from only one single RGB natural image using a pyramid of fully convolution generative networks, each learns data distribution at different scale from coarse to fine. It used in various image manipulation tasks such as super-resolution, paint to image, harmonization, editing an animation. This method is based on learning internal structure of one image and can not be used to have high quality images, but can not be applicable with complex, diverse and high dimensional data related to other data (e.g, in geophysical and astrophysical applications). Emily *et. al* [4] also used a cascade of convolution network with a Laplacian pyramid of conditional generative networks to generate images with higher quality. It is used in different datasets for fidelity propose.

In astrophysics, Taeyoung *at el.* [10] used image-to-image translation conditional generative model [8] to generate frontside solar magnetograms from SDO [16]/AIA [12] and then from STEREO [9]/EUVI [7] data. It uses ImageGAN as a discriminator architecture, that only focuses on global structure in input image ignoring high-frequencies structure.

In this paper, the goal is to improve the previous work using multi-layer conditional generative adversarial model to capture internal distribution from global to local polarity structure which is not well generated in previous method. The generative model consists of hierarchical generators and discriminators that use PatchGAN classifier to capture coarse and fine details. Therefore, discriminators classify overlapping patches and average all outputs.

3. Method

The goal of this work is to capture global and local bipolar structure behind both AIA [12] and EUVI [7] images. The training step is based on learning internal structure behind AIA [12] image (X) to generate frontside HMI [18] magnetogram ($\tilde{Y}$) based on true frontside HMI magnetogram (Y). The generative framework consists of multi-scale layers, each consists of one generator and discriminator starting from low-resolution image to higher-resolution image. All discriminators in all layers use PatchGAN (Markovian discriminator) [8]; starting from coarsest to finest patch-size to differentiate hierarchical structure in the input image (Y) and predicted image ($\tilde{Y}$). The hierarchy of PatchGAN is applied to capture global structures (e.g., large polarity structure) in addition to small details (e.g, ting polarity structure); each is responsible of capturing the patch distribution at a different scale. The training samples are patches, rather than whole images. Figure 2 shows the architecture of generative adversarial model.

3.1. Multi-layer Architecture

The generative adversarial network consists of a hierarchy of generators (G) and discriminators (D):

$$G = \{G_0, G_1, ..., G_M\}, \tag{1}$$

$$D = \{D_0, D_1, ..., D_M\}, \tag{2}$$

Where M is the number of hierarchical layers in the network's architecture. Each generators G_m at finer scales add more details, which is not generated by the previous coarser scale G_{m-1}. The input data (X, Y) is a sequence of input images and their ground-truth images (e.g., AIA and HMI) in all layers.

$$(X, Y) = \sum_{m=0}^{m=M-1} \sum_{n=0}^{n=N-1}, (x_m^n, y_m^n), \tag{3}$$

Where x_m^n and y_m^n are up-sampled version of x_{m-1}^n and y_{m-1}^n of sample index n by factor $f_m = 1/2$. Both x_m and y_m are up-sampled. To simplify, x_m^n, y_m^n will be referred as x_m, y_m.

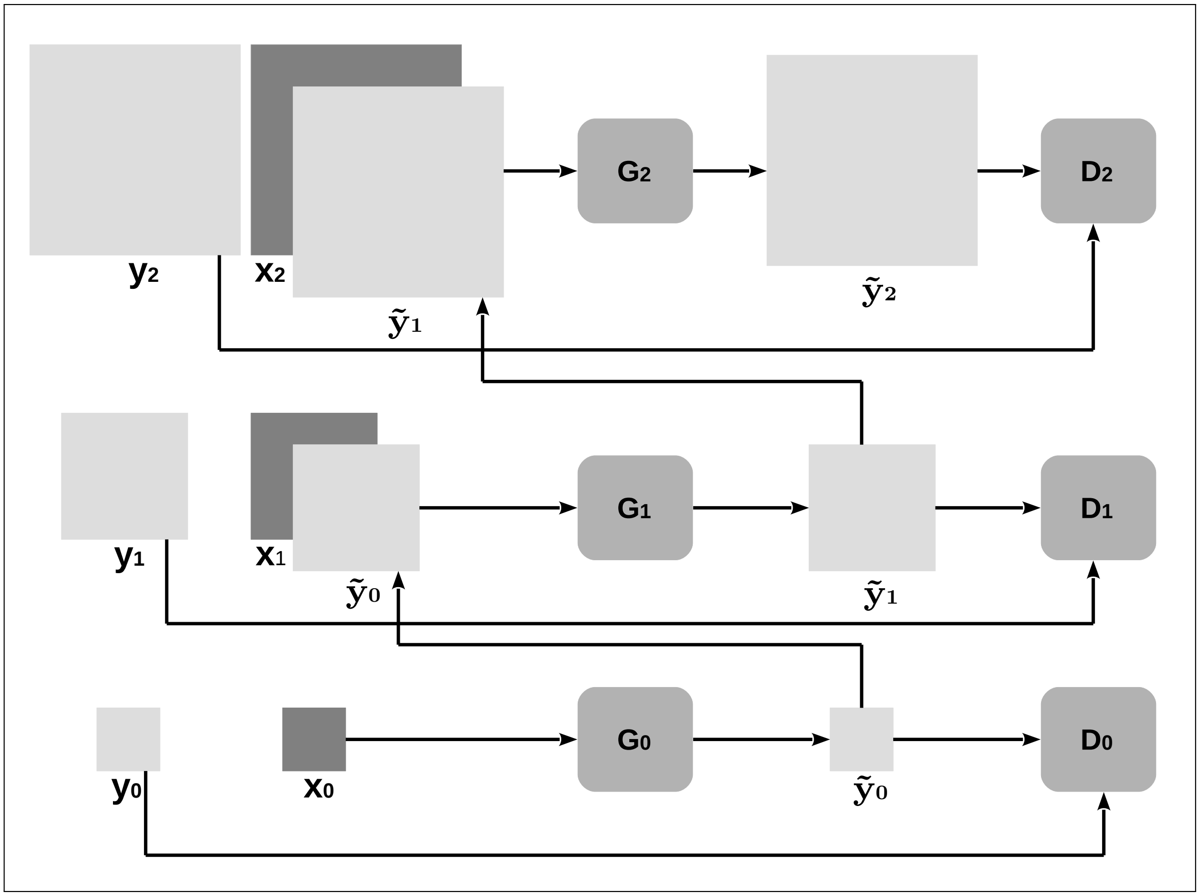

Figure 2. Multi-layer architecture. The generative model consists of 3 layers of generators and discriminators. In each layer, generator (G) learns to generate image sample and discriminator (D) learns to differentiate between true image sample and generated sample. Each x, y and $\tilde{y}$ present input image, ground-truth and generated images from each layer.

The input of the first generator G_0 is input data x_0. The input of other generator G_m are input data x_m and generated image from previous layer $\tilde{y}_{m-1}\uparrow$ after up-sampled to the size of x_m:

$$\tilde{y}_0 = G_0(x_0), \tag{4}$$

$$\tilde{y}_m = G_m(x_m, \tilde{y}_{m-1}\uparrow), \tag{5}$$

The input of all discriminators D_m is a pair of (x_m, y_m) and a pair of $(x_m, \tilde{y}_m)$. The discriminators start with largest patch size (in D_0) to smallest patch size (in D_M) as they pass though all layers to capture hierarchical structure from corset to finest details. The patch size of the first discriminator (D_0) equal to $f_p = 1/2$ of the image's width.

All generators G_m in hierarchical layers have same architecture. It use modified version of uNet architecture. It consists of 6 convolution blocks, which consists of convolution, batch normalization and LeaklyReLU activation. It also consists of 6 dconvolution blocks, which consists of dconvolution, batch normalization and ReLU activation in addition to skip-connection. It starts with 64 filter kernels of size (4×4). All discriminator networks D_m also have same architectures in all layers. It consisting of 6 convolution blocks, which consists of convolution, batch normalization and LeaklyReLU activation; starting with 64 kernels of size (4×4).

3.2. Training

The generative adversarial model is trained starting from smallest input image x_0 and largest patch size. The training loss of multi-layer architecture comprises of classical conditional GAN loss:

$$\begin{aligned} L_{cGAN}(G_m, D_m) = E_{(x_m,y_m)}\left[log(D_m(x_m, y_m))\right] \\ +E_{(x_m,\tilde{y}_m)}\left[log(1 - D_m(x_m, \tilde{y}_m))\right], \end{aligned} \tag{6}$$

Where G_m minimizes the previous objective function against adversarial D_m in each layer m. D_m penalizes the distance between the distribution of ground-truth image y_m and generated data $\tilde{y}_m$. Binary cross-entropy and l2 losses are used as adversarial loss and reconstruction loss in each layer to differentiate between y and $\tilde{y}$ with weight λ:

$$L_{l2}(G_m) = E_{(x_m,y_m)}\left[(\tilde{y}_m - y_m)^2\right], \quad (7)$$

The final training loss of generative adversarial model can be presented as:

$$G^{\star} = \arg\min_{G_m}\max_{D_m} L_{cGAN}(G_m, D_m) + \lambda L_{l2}(G_m), \quad (8)$$

4. Experiments

4.1. Data

AIA [12] and HMI [18] data are obtained from the SDO [16] data center (https://sdo.gsfc.nasa.gov/) of Joint Science Operations Center (http://jsoc.stanford.edu/) with 12-hours cadence. AIA data is generated by AIA instrument with wavelength 304 angstrom (observing transition region of solar atmosphere, called chromosphere) with $4096 \times 4096 \times 1$ pixel; each 12 um pixel corresponds to 0.6 arcsec. HMI data is generated by HMI instrument which is used to measure line-of-sight magnetic field at the solar photosphere using 6173 magnetogram with $2046 \times 2046 \times 1$ pixel; each 12 um pixel corresponds to 0.5 arcsec. EUVI [7] data of STEREO B Observatory are obtained from STEREO Science Center (https://stereo.gsfc.nasa.gov/) with 12-hours cadence. This data is generated by Sun-Earth-Connection Coronal and Heliospheric Investigation (SECCHI) instrument with wavelength 304 angstrom with $2048 \times 2048 \times 1$; each 12 um pixel corresponds to 1.59 arcsec. The data is splitted into two parts. The training data comprises of data between January 2011 and December 2019, excluding September and October. The testing data comprises of data from September and October between 2011 and 2019 of AIA/HMI pairs. To generate farside magnetograms, EUVI data is only available before 1 October 2014 from January 2010 and doesn't have ground-truth magnetograms. 4800 pairs of AIA/HMI images are selected to train network and 950 pairs of AIA/HMI images are selected to evaluate generator. All AIA, HMI and EUVI images are resized using bi-cubic interpolation into $512 \times 512 \times 1$. The range values of AIA between -7.89 ± 1.29 to 4254.78 ± 5539.56, HMI between -4764.16 ± 211.57 to 4764.16 ± 211.57 and EUVI between 656.8 ± 1.6 to 13392.8 ± 3695.36.

4.2. Preprocessing and Experimental Setting

Preprocessing involves four main steps: projection, masking, linear stretching and normalization. Image projection is used to align HMI with AIA data and align EUVI with AIA data. Binary mask is applied to AIA, HMI and AIA images to remove effects of background pixels by equalization background pixels to minimum values. Linear stretching and normalization are used to reduce low contrast between solar pixels. AIA and EUVI data is normalized using 98% percentage and HMI data is normalized using z-scale. Then all images are normalized between -1 and 1 as inputs to generative networks.

Tanh and sigmoid are used as last activation function of generator and discriminator, respectively. Adam optimization function with learning rate equal 0.0002 and momentum parameter $B_1 = 0.5$ and $B_2 = 0.999$ is applied with mini-batch SGD. The experiment starts with the weights of Gaussian distribution with mean 0 and standard deviation 0.02.

The size of the input image of the first generator G_0 is $128 \times 128 \times 1$ (X_0), second generator G_1 is $256 \times 256 \times 1$ (X_1) and third generator G_2 is $512 \times 512 \times 1$ (X_2). The size of the input patch of the first discriminator (D_0) is 64×64, second discriminator (D_1) is 32×32 and third discriminator (D_2) is 16×16. The network is trained for 100000 epochs with batch size 1. All experiments are run on Nvidia Tesla V100 GPUs-32 GB with Keras 2 of Tensorflow 1.4.

4.3. Evaluation Metrics

Ground-truth HMI is compared with generated HMI magnetograms. Some metrics of previous work [10], which uses image to image translation with conditional GAN [8], are used to compare the performance with previous one. Pixel to pixel correlation coefficient (CC), total unsigned of magnetic flux [15] correlation coefficient (CC), relative error (R1) of the total unsigned magnetic flux [1] and normalized mean square error (R2) of the magnetic field [1] between HMI and generated HMI are used. In additional to previous metrics, the average of root mean squared error (RMSE) and the structural similarity index (SSIM) [2, 17] (higher better quality) is used, as shown in Eq. 9. Peak signal-to-noise ratio (PSNR) [2] (higher better quality) are also used.

$$E(y, \tilde{y}) = \frac{RMSE(y, \tilde{y}) + (1 - |SSIM(y, \tilde{y})|)}{2}, \quad (9)$$

4.4. Results

4.4.1 Comparison between the proposed GAN and previous method

The model is evaluated using a pair of AIA and HMI images from 2011 to 2019 during September and October. Figure 3 shows AIA, true HMI, generated HMI from previous method [10] and generate HMI of the proposed model in the first, second, third and four row, respectively. It presents solar observations each 2 days at 12:00 UT (Universal Time): 1 September 2017 12:00 UT, 3 September 2017 12:00 UT, 5 September 2017 12:00 UT and 7 September 2017 12:00 UT. In both cases, bipolar structure is restored; however previous method does not generate small details and reverses between magnetic fields around active region (reverses white

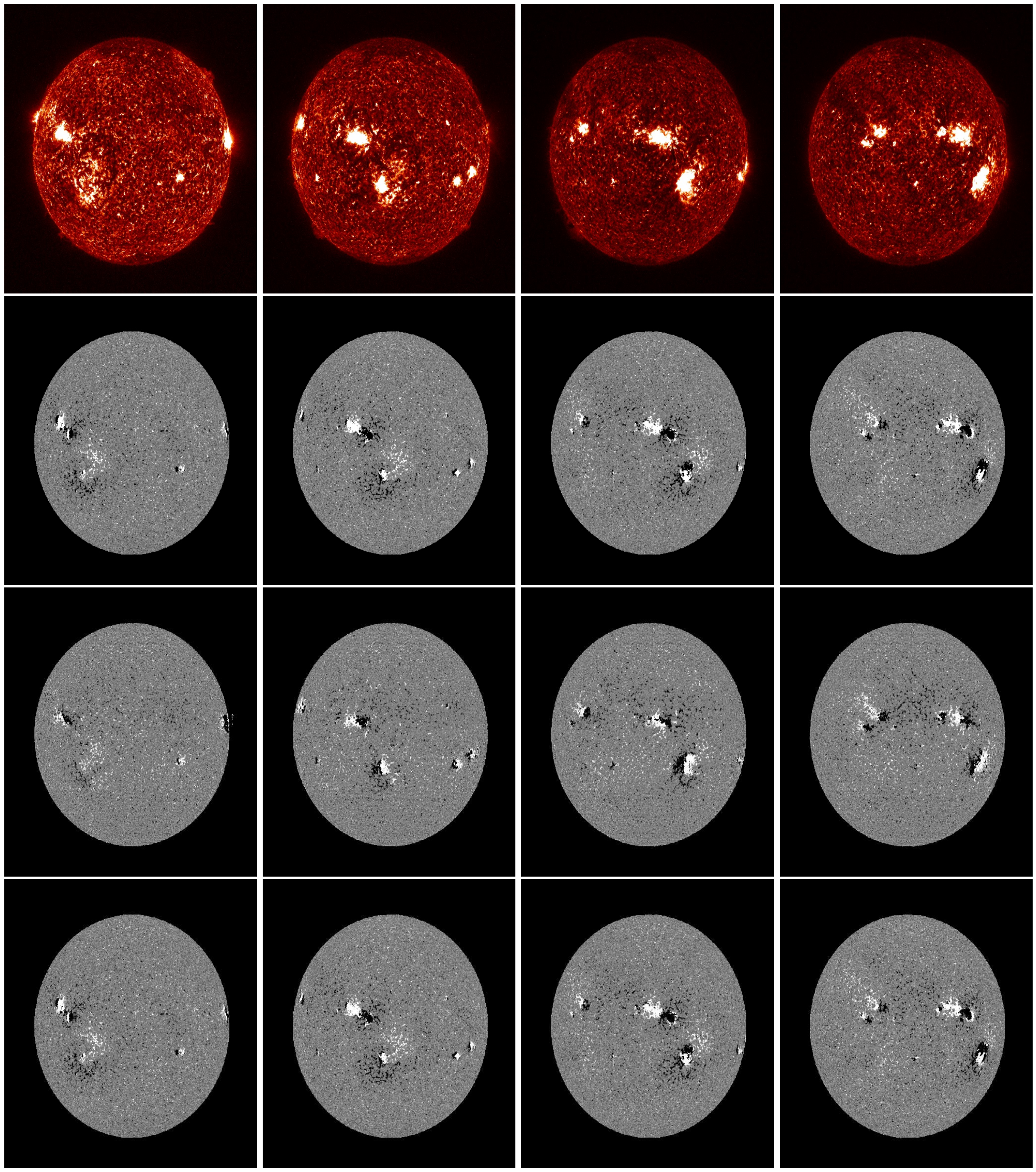

(a) 1 Sept 2017 12 UT **(b) Sept 2017 12 UT** **(c) Sept 2017 12 UT** **(d) Sept 2017 12 UT**

Figure 3. Comparison between HMI and generated HMI magnetograms from AIA $304-\mathring{A}$ for 1 September 2017 12:00 UT, 3 September 2017 12:00 UT, 5 September 2017 12:00 UT and 7 September 2017 12:00 UT with 2 days cadence. The input AIA image, HMI, generated HMI from [10] and generated HMI magnetograms from the proposed model are presented in first, second, third and fourth rows, respectively.

and back areas in addition to over/under estimation of these areas). The proposed method detects smaller details in quiet regions and properly generates polarity patterns in active regions due to hierarchical architecture with increasing image size and decreasing patch size, which helps to capture difference in patterns and preserve local and global structures.

The performance of the proposed and previous generative networks [10] in 950 pairs of AIA and HMI is measured based on physical properties (e.g., total unsigned magnetic flux and magnetic field) and image properties (e.g., SSIM and PSNR) in Table 1. Taeyoung *et al.* [10] use ImageGAN of full disk of AIA and HMI images (first column), as mentioned previously in Section 2. In order to compare with the proposed model, PatchGAN (64×64) is applied to the previous network (second column). PatchGAN (64×64) of multi-layer architecture (third column) and

Method	Taeyoung *et. al.*		Proposed	
	Image	Patch 64×64	Patch 64×64	multi-patch
Pixel2Pixel CC	0.85	0.89	0.90	0.94
Total unsigned magnetic flux CC	0.59	0.64	0.75	0.89
Total unsigned magnetic flux-R1	0.091 ± 0.079	0.080 ± 0.059	0.070 ± 0.019	0.050 ± 0.007
Magnetic field -R2	0.055 ± 0.005	0.045 ± 0.005	0.040 ± 0.032	0.011 ± 0.007
RMSE-SSIM	0.82 ± 0.032	0.85 ± 0.022	0.87 ± 0.01	0.90 ± 0.01
PSNR	17.74 ± 1.19	15.74 ± 1.19	14.00 ± 1.21	11.14 ± 1.21

Table 1. Comparison between previous model [10] and proposed model.

then multiple PatchGAN starting from 64×64 (fourth column) are used. It is remarkable that applying PatchGAN improves the performance of the previous network. Pixel-to-pixel CC and total unsigned magnetic flux CC of PatchGAN are increased from 0.85 and 0.59 to 0.89 and 0.64, respectively. In addition, errors of unsigned magnetic flux and magnetic field are reduced by 10% and image qualities (RMSE-SSIM and PSNR) are improved. These imply that solar magnetograms are better generated using PatchGAN. However, using multi-layer architecture with standard patch size or multiple patch size demonstrates better estimation of physical properties (higher correction coefficient and lower error) and higher quality (RMSE-SSIM=0.90 ± 0.01 and PSNR=11 ± 1.21) of generated images.

The model is also evaluated using EUVI $304 - \mathring{A}$ after projecting with AIA $304 - \mathring{A}$. Generated magnetograms is not compared with true magnetograms because farside solar magnetograms are not available, as mentioned previously in Section 4.1. Active regions from farside to frontside observations are temporally monitored each 3 days at 00:00 UT. Figure 4 shows 2 EUVI images in 14 September 2014 and 17 September 2014 (a and b) and then AIA images in 20 September 2014 and 23 September 2014 (c and d). In both cases, bipolar patterns around active regions are conserved and are moved from farside images (a and b) to appear in frontside images (c and d).

4.4.2 Comparison between ImageGAN and PatchGAN in multi-layer architectures

Figure 5 shows results of applying ImageGAN and PatchGAN. Fig. 5(b) is an output of applying baseline architecture. Fig. 5(c) is an output of applying multi-layer architecture, where the input data of discriminators is image size; image size is depending in which level in the architecture. Fig. 5(d) is a result of multi-layer architecture, where the input data of discriminators is hierarchical patch-size; starting from largest size to smaller size. It is noticed from (c) and (d) that multi-layer architecture succeeds to restore most global and small structure. On other hand, generated HMI magnetograms from ImageGAN (c) miss tiny difference in bipolar structure around some active regions (white area (positive magnetic polarity) is underestimated to black area (negative magnetic polarity) or reverse), which could be important to study active region properties (e.g, magnetic flux, current helicity) if it is predicted correctly. White regions present magnetic field pointing out of the Sun, black regions shows magnetic field pointing into the Sun and ting flux elements that cover most of gray area are results of HMI extraordinary capabilities. In general, precisely prediction of ting black and white regions is important because they are the basis for coronal loop and prominences in the solar atmosphere (e.g., AIA) and many solar activities (e.g., flares and coronal mass ejections) which can effect negatively on the Earth.

4.4.3 Comparison between uNet and other generator architectures

Multi-layer generative model is evaluated using different end-to-end architectures as generators. Simplified version of ResNet [6], encoder-decoder with astrous convolution [3] and uNet are applied. ResNet network is composed of one encoder block and five residual blocks and one decoding block. Each encoding/decoding block consists of convolution/deconvolution, instance-norm, ReLU. Each residual block consists of convolution, instance-norm, convolution and instance-norm residual connection. Encoder-decoder with astrous convolution applies spatial pyramid pooling to the encoder-decoder architecture. Table 2 illustrates that encoder-decoder with astrous convolution and ResNet have better interpretation of physical variables; high correlation coefficients of pixel2pixel and unsigned magnetic flux with low error in unsigned magnetic flux and magnetic field. In addition, they have better image quality (high RMSE-SSIM and low PSNR). Usually, ResNet network is effective because of residual connections. On other hand, encoder-decoder with astrou convolution captures the contextual information by pooling features at different resolution. In this case, most active regions (black/white areas from gray area) have sharp change in magnetic field values from positive to negative or reverse, where this network can interpret. Magnetic flux is a result of multiplying magnetic area (number of magnetic pixel) with magnetic field; better estimation of

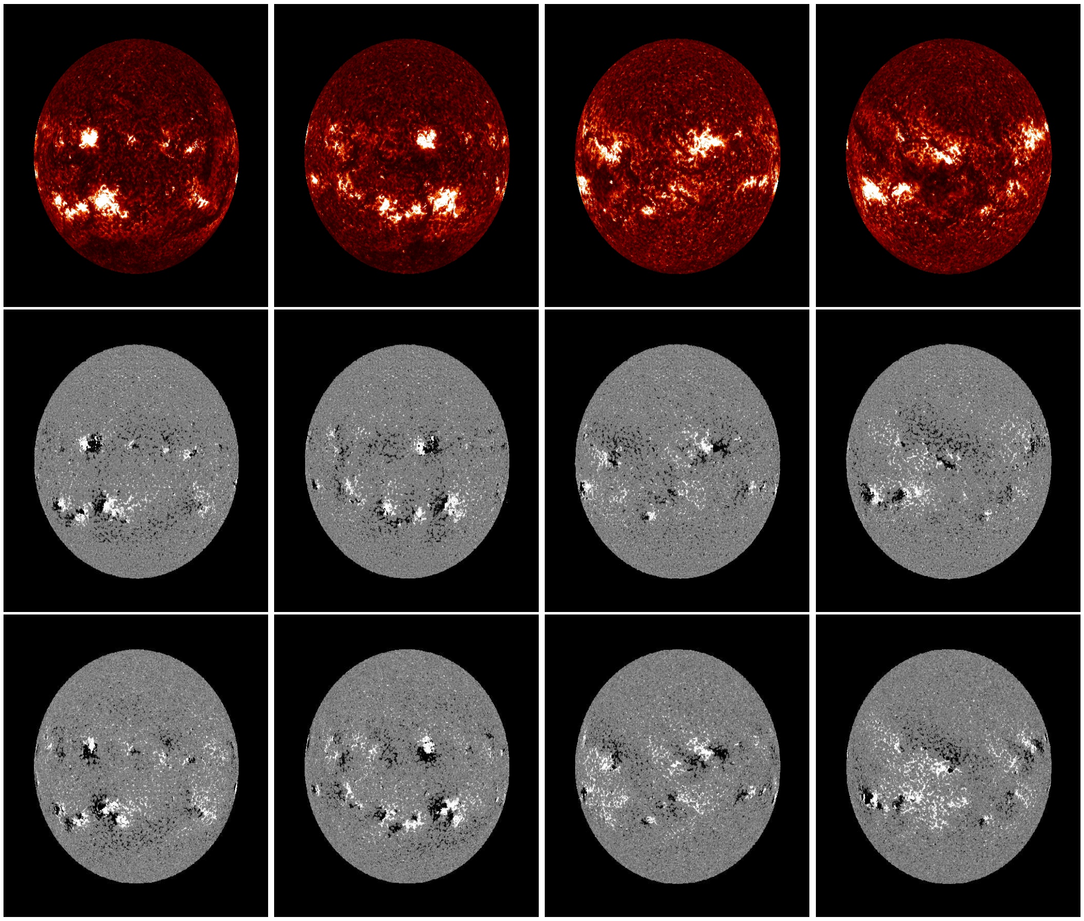

(a) 14 Sep 2014 00 UT (b) 17 Sep 2014 00 UT (c) 20 Sep 2014 00 UT (d) 23 Sep 2014 00 UT

Figure 4. Comparison between HMI and generated HMI magnetograms from EUVI $304-\mathring{A}$ for 14 September and 17 September 2014 and AIA $304-\mathring{A}$ for 20 September and 23 September 2014 with 3 days cadence. The first and second images are EUVI images and third and fourth images are AIA images in the first row. solar magnetograms from [10] and generated solar magnetograms from the proposed model are presented in second row and third row, respectively.

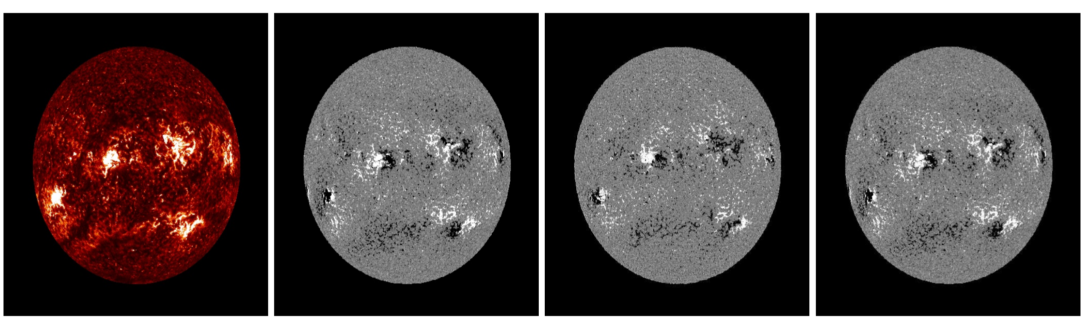

(a) AIA (b) HMI (c) HMI-ImageGAN (d) HMI-PatchGAN

Figure 5. Comparison between generated HMI magnetograms after applying ImageGAN and PatchGAN in multi-layer architecture. AIA, ground-truth HMI, generated HMI of ImageGAN and of PatchGAN are presented in the first, second, third and fourth images, respectively (23 Oct 2012 12:00 UT).

magnetic field means better estimation of magnetic flux.

Method	Encoder-Decoder with Astrou Convolution	ResNet	uNet
Pixel2Pixel CC	0.95	0.93	0.94
Total unsigned magnetic flux CC	0.90	0.89	0.89
Total unsigned magnetic flux-R1	0.043 ± 0.52	0.048 ± 0.44	0.050 ± 0.007
Magnetic field -R2	$0.021 \pm .32$	0.010 ± 0.23	0.011 ± 0.007
RMSE-SSIM	$0.90 \pm .0.31$	0.92 ± 0.21	0.90 ± 0.01
PSNR	9 ± 3.11	8.32 ± 5.12	11.14 ± 1.21

Table 2. Comparison between generator's architecture: encoder-decoder with astrou convolution, ResNet and uNet.

5. Summary and Future Work

In this work, a multi-layer generative model is proposed, which uses PatchGAN to learn local and global structure from hierarchical input data. Its ability to generate bipolar structure of solar magnetograms is demonstrated from coarsest to finest scale. The goal is to continue this work to reproduce physical variables by using synthetically generated images. The proposed model is trained and evaluated for 24th solar cycle (12-hours cadence :00 UT and 12 UT). It may more effective to train each 3, 6 or 9 hours cadence (odd solar cycle) and evaluate for different cycle 4 ,8 or 12 hours cadence (even solar cycle). This work shows image-to-image translation between different sensors. The AIA image instrument provide imaging observations of solar photosphere, chromosphere and corona in 2 Ultraviolet and 7 Extreme Ultraviolet channels (e.g., AIA $171-\mathring{A}$, AIA $192-\mathring{A}$, AIA $211-\mathring{A}$); each presents a certain wavelength. This work can be extend to include observations with various wavelengths to improve fidelity of other observations in active regions (e.g., AIA $211-\mathring{A}$ and AIA $335-\mathring{A}$) and consequently reproduce physical variables by using generated images.

Acknowledgements

The author thanks team members of the SDO mission and STEREO mission and acknowledge effort devoted to develop open-source python packages: Sunpy and Keras. This work is supported by the New York University, Abu Dhabi Kawader Research Program. Computational resources are provided by HPC center in the New York university, Abu Dhabi.

References

[1] M. G. Bobra, X. Sun, J. T. Hoeksema, M. Turmon, Y. Liu, K. Hayashi, G. Barnes, and K. D. Leka. The Helioseismic and Magnetic Imager (HMI) Vector Magnetic Field Pipeline: SHARPs - Space-Weather HMI Active Region Patches. *Solar Physics*, 289(9):3549–3578, 2014.

[2] Ali Borji. Pros and Cons of GAN Evaluation Measures. *Computer Vision and Image Understanding*, 179:41–65, 2019.

[3] Liang-Chieh Chen, Yukun Zhu, George Papandreou, Florian Schroff, and Hartwig Adam. Encoder-Decoder with Atrous Separable Convolution for Semantic Image Segmentation. In *European Conference on Computer Vision*, 2018.

[4] Emily L Denton, Soumith Chintala, Arthur Szlam, and Rob Fergus. Deep Generative Image Models Using a Laplacian Pyramid of Adversarial Networks. In *Advances in Neural Information Processing Systems 28*, pages 1486–1494. 2015.

[5] Ian Goodfellow, Jean Pouget-Abadie, Mehdi Mirza, Bing Xu, David Warde-Farley, Sherjil Ozair, Aaron Courville, and Yoshua Bengio. Generative Adversarial Nets. In *Advances in Neural Information Processing Systems 27*, pages 2672–2680. 2014.

[6] Kaiming He, Xiangyu Zhang, Shaoqing Ren, and Jian Sun. Deep Residual Learning for Image Recognition. In *IEEE Conference on Computer Vision and Pattern Recognition*, pages 770–778, 2016.

[7] Russell Howard, J.D. Moses, Angelos Vourlidas, J. Newmark, D. Socker, S. Plunkett, C. Korendyke, J.W. Cook, A. Hurley, Joseph Davila, W.T. Thompson, O.C. Cyr, E. Mentzell, Ivy Kimberly, R. Lemen, J.P. Wuelser, D.W. Duncan, Ted Tarbell, C.J. Wolfson, and T Carter. Sun Earth Connection Coronal and Heliospheric Investigation (SECCHI). 2008.

[8] P. Isola, J. Zhu, T. Zhou, and A. A. Efros. Image-to-Image Translation with Conditional Adversarial Networks. In *IEEE Conference on Computer Vision and Pattern Recognition*, pages 5967–5976, 2017.

[9] M.L. Kaiser, T.A. Kucera, Joseph Davila, O. St. Cyr, Madhulika Guhathakurta, and Eric Christian. The STEREO Mission: an Introduction. *Space Science Reviews*, 136:5–16, 2008.

[10] Taeyoung Kim, Eunsu Park, Harim Lee, Yong-Jae Moon, and Sung-Ho Bae. Solar Farside Magnetograms from Deep Learning Analysis of STEREO/EUVI Data. *Nature Astronomy*, 3:397–400, 2019.

[11] C. Ledig, L. Theis, F. Huszár, J. Caballero, A. Cunningham, A. Acosta, A. Aitken, A. Tejani, J. Totz, Z. Wang, and W. Shi. Photo-Realistic Single Image Super-Resolution Using a Generative Adversarial network. In *IEEE Conference on Computer Vision and Pattern Recognition*, pages 105–114, 2017.

[12] James Lemen, Alan Title, Paul Boerner, Catherine Chou, Jerry Drake, Dexter Duncan, Christopher Edwards, Frank Friedlaender, Gary Heyman, Neal Hurlburt, Noah Katz, Gary Kushner, Michael Levay, Russell Lindgren, Dnyanesh

Mathur, Edward McFeaters, Sarah Mitchell, Roger Rehse, and Nick Waltham. The Atmospheric Imaging Assembly (AIA) on the Solar Dynamics Observatory (SDO). *Solar Physics*, 275:17–40, 2011.

[13] C. Lindsey, Braun, and D. C. Seismic Images of the Far Side of the Sun. *Science*, 287(5459):1799–1801, 2000.

[14] Charles Lindsey and Douglas Braun. Seismic Imaging of the Sun's far Hemisphere and Its Applications in Space Weather Forecasting. In *Space weather : the International Journal of Research and Applications*, 2017.

[15] P.C.H. Martens, G.D.R Attrill, A.R. Davey, A Engell, S Farid, P.C. Grigis, J. Kasper, K. Korreck, S.H. Saar, A. Savcheva, Y. Su, P. Testa, M. Wills-Davey, P.N. Bernasconi, N.-E. Raouafi, V.A. Delouille, J.F. Hochedez, J.W. Cirtain, C.E. DeForest, R.A. Angryk, Ineke De Moortel, T. Wiegelmann, M.K. Georgoulis, R.T.J. McAteer, and R.P. Timmons. Computer Vision for the Solar Dynamics Observatory (SDO). *Solar Physics*, 275:79–113, 2012.

[16] William Pesnell, Barbara Thompson, and Phillip Chamberlin. The Solar Dynamics Observatory (SDO). *Solar Physics*, 275:3–15, 2012.

[17] Valentina Salvatelli, Souvik Bose, Brad Neuberg, Luiz Fernando Guedes dos Santos, Mark Cheung, Miho Janvier, Atilim Baydin, Yarin Gal, and Meng Jin. Using U-Nets to Create High-Fidelity Virtual Observations of the Solar Corona. In *Conference on Neural Information Processing Systems*, 2019.

[18] Jørgen Schou, Philip H. Scherrer, Rock Irvin Bush, Richard Wachter, S'ebastien Couvidat, Maria Cristina Rabello-Soares, Richard S. Bogart, J T Hoeksema, Y. Liu, T. L. Jr. Duvall, Demir Akin, Bart A. M. Allard, John Wesley Miles, R. Rairden, Richard A. Shine, Theodore D. Tarbell, Alan M. Title, C. Jacob Wolfson, David F. Elmore, A. A. Norton, and Steven Tomczyk. Design and Ground Calibration of the Helioseismic and Magnetic Imager (HMI) Instrument on the Solar Dynamics Observatory (SDO). *Solar Physics*, 275:229–259, 2012.

[19] Tamar Rott Shaham, Tali Dekel, and Tomer Michaeli. SinGAN: Learning a Generative Model from a Single Natural Image. In *IEEE International Conference on Computer Vision*, 2019.

[20] Jun-Yan Zhu, Taesung Park, Phillip Isola, and Alexei A Efros. Unpaired Image-to-Image Translation Using Cycle-Consistent Adversarial Networkss. In *IEEE International Conference on Computer Vision*, 2017.